NANO LETTERS

LETTER

pubs.acs.org/NanoLett

All-Optical Control of a Single Plasmonic Nanoantenna—ITO Hybrid

Martina Abb,[†] Pablo Albella,[‡] Javier Aizpurua,[‡] and Otto L. Muskens*[,†]

[†]SEPnet and the Department of Physics and Astronomy, University of Southampton, Highfield, Southampton SO17 1BJ, United Kingdom

[‡]Donostia International Physics Center, DIPC, and Centro de Fisica de Materiales CSIC-UPV/EHU, Paseo Manuel Lardizabal 4, Donostia-San Sebastian 20018, Spain

ABSTRACT: We demonstrate experimentally picosecond all-optical control of a single plasmonic nanoantenna embedded in indium tin oxide (ITO). We identify a picosecond response of the antenna—ITO hybrid system, which is distinctly different from transient bleaching observed for gold antennas on a nonconducting SiO_2 substrate. Our experimental results can be explained by the large free-carrier nonlinearity of ITO, which is enhanced by plasmon-induced hot-electron injection from the gold nanoantenna into the conductive oxide. The combination of tunable antenna—ITO hybrids with nanoscale plasmonic energy transfer mechanisms, as demonstrated here, opens a path for new ultrafast devices to produce nanoplasmonic switching and control.

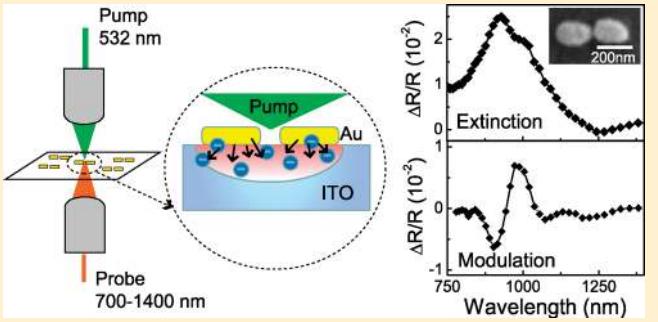

KEYWORDS: Active, plasmonic, nanoantenna, hybrid nanostructures, nanophotonics

Nanophotonic devices that can efficiently concentrate optical radiation into a nanometer-sized volume are of great interest for many applications in integrated and nonlinear photonics, radiative decay engineering, and quantum information processing. In plasmonics, ultrasmall mode volumes and high local field enhancement are achieved by exploiting the surface plasmon resonances of metal nanostructures. Analogous to radiowave antennas, plasmonic nanoantennas have been developed, providing a high local field enhancement with efficient coupling to far field radiation.[1,2] Active control of the resonance spectrum of a plasmonic nanoantenna is a crucial step toward achieving transistor-type nanodevices for manipulation of the flow and emission of light. Such active nanoplasmonic devices may hold promise for on-chip integration of optical and electronic functionalities.[3,4] A variety of schemes have been proposed and developed to control plasmonic modes using optical, electrical, magnetic, thermal, or mechanical means.[5−19] While propagating surface plasmon polaritons provide a long interaction length, allowing switching at modest intensities,[9−13] localized mode switching may benefit from the design of nanoplasmonic modes with strong local field enhancement and high sensitivity to refractive index changes.[14−20] Large modulation has been obtained recently for plasmonic nanoantennas using an electrically controlled liquid crystal.[18,19] While liquid crystals provide sizable tuning of the antenna response, the temporal response is too slow for many applications. Furthermore, a solid-state implementation would be favorable for on-chip integration of nanoplasmonic devices.

Here, we demonstrate all-optical control of plasmon modes of individual nanoantennas using the nonlinear response of a nanoantenna—ITO hybrid. Transparent conductive oxides have recently been identified as promising materials for plasmonics and transformation optics applications in the near-infrared spectrum.[21] Unity-order changes of the refractive index of indium tin oxide (ITO) above its bulk plasmon frequency have been demonstrated using voltage-controlled nanoscale space charge regions.[22] The free-carrier density of ITO can be varied through the concentration of Sn^{4+} dopants and through oxygen vacancies introduced at higher deposition temperatures.[23,24] The plasmon frequency is directly proportional to the free-carrier density and is located in the near-infrared range at a wavelength of $\sim 1\ \mu m$ for carrier densities around $10^{21}\ cm^{-3}$.[25] In this work we explore picosecond optical excitation of ITO as a means for locally modulating the free-carrier density. In particular, we investigate the mutual interaction of the plasmonic nanoantenna, which acts as a local source for sensitizing the ITO response, and the ITO free-carrier nonlinearity which in return modifies the plasmon resonance. We show that this rapid energy transfer mechanism results in a sizable modulation of the dipolar mode of a single plasmonic nanoantenna.

Gold nanoantennas were fabricated using standard electron-beam lithography on an ITO-coated glass substrate. Two types of commercial ITO substrates (Sigma-Aldrich) were used: a 25 nm thick ITO layer with sheet resistivity of 70—100 Ω/square ("low-conductivity"), and a 120 nm thick ITO with sheet resistivity of 8—12 Ω/square ("high-conductivity"). Nanoantennas were fabricated using deposition of a gold layer of 25 nm followed by liftoff. We produced samples of nanoantennas on high- and low-conductivity ITO both with and without a cover layer of ITO.

Received: March 18, 2011
Revised: April 25, 2011

   dx.doi.org/10.1021/nl200901w | *Nano Lett.* XXXX, XXX, 000–000

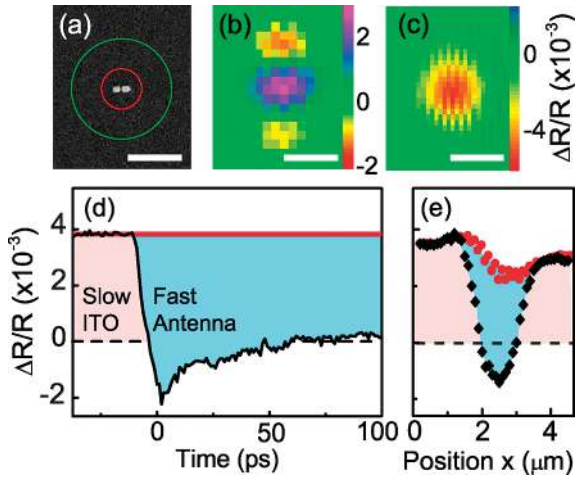

Figure 1. (a) SEM image of dimer nanoantenna, circles indicating size of the pump (green) and the probe (red) spots. Microscopy images of (b) antenna extinction (spatial modulation) signal and (c) fast component of nonlinear pump−probe signal (thermal background subtracted) at 180 pJ pump energy. Scale bars in panels a−c, 1 μm. (d) Time-resolved reflectivity, at 910 nm wavelength, of nanoantenna with slow (red color) and fast antenna−ITO hybrid response (blue color). (e) Cross sections of nonlinear signal at $t = -20$ ps (red circles) and pump−probe signal at $t = 5$ ps (black diamonds), blue color indicating the fast nonlinear component.

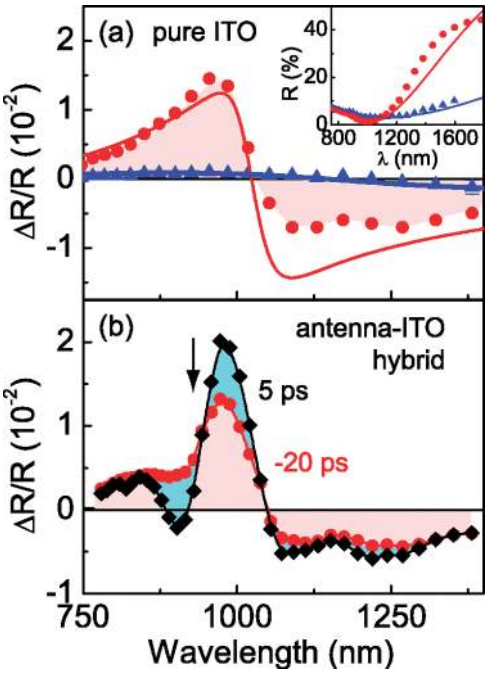

Figure 2. (a) Slow nonlinear response from the high conductivity (red circles) and low conductivity (blue triangles) ITO substrates, with (inset) reflectivity. Lines indicate Drude model calculations. (b) Slow (red shaded area) and fast (blue shaded area) pump−probe response from a nanoantenna surrounded by high-conductivity ITO, nominal gap size 20 nm. The vertical arrow indicates the maximum of the antenna resonance as shown in Figure 3a. Pump energy was 180 pJ for both panels a and b.

For covered antennas, a 25 nm thick ITO layer was deposited with a sheet resistivity matched to the respective ITO substrates. High conductivity ITO with a sheet resistance of 20 Ω/square was obtained by radio frequency (rf) sputtering in an oxygen/argon plasma with a mixing ratio of 1:136 at a temperature of 490 °C. Low conductivity ITO with a sheet resistance of 150 Ω/square was obtained by rf sputtering in an oxygen/argon plasma at a temperature of 300 °C using the same mixing ratio.

For the linear and ultrafast spectroscopy of individual nanoantennas, we used an ytterbium fiber laser amplifier (Fianium, Ltd.) with a repetition rate of 40 MHz, providing optical pulses of 4 ps duration. The pump beam was frequency doubled to a wavelength of 532 nm using a KTP crystal of 5 mm thickness and was focused onto a single antenna through the substrate side using a 0.6 NA aspheric lens. As a probe we used a broad band supercontinuum generated in a photonic crystal fiber. Parts of the broad band supercontinuum spectrum, spanning 460−1800 nm and with an integrated optical power of around 2 W, were selected using a subtractive mode double prism monochromator. The probe was focused by a microscope objective (Mitutoyo 100× NIR, 0.5 NA) onto the front side of the sample. The focal spots at the sample were obtained from camera images as 0.7 μm fwhm for the probe around 900 nm wavelength and 2.0 μm for the pump, as indicated by the circles in Figure 1a. The highest pump energy used amounted to 180 pJ per pulse, which corresponds to a fluence of 5.7 mJ/cm^2 at the sample.

The plasmonic modes of individual nanoantennas are characterized using the method of spatial modulation microscopy (SMM).[26,27] SMM produces very sensitive extinction measurements by detecting a periodical modulation of the particle position in the laser focus using a lock-in amplifier. The nanoantennas are located using two-dimensional SMM scans as shown in Figure 1b. The spatial modulation is chosen perpendicular to the antenna long axis to reduce finite-antenna size effects in the SMM response.

The typical observed three-peak profile for a single antenna is characteristic for SMM when using lock-in detection at the second harmonic of the modulation frequency. The central peak value is directly proportional to the extinction cross section of the antenna and can be used to obtain a single-particle extinction spectrum,[27] as will be shown below. After identification of a single nanoantenna using its optical extinction signature, we measured its picosecond nonlinear response following excitation by the pump laser. A nonlinear response was observed from both the nanoantenna and the ITO substrate, as illustrated in Figure 1c−e. Figure 1d shows the time-resolved nonlinear response measured at the position of the nanoantenna, at a wavelength of 910 nm. The differential reflectivity signal $\Delta R/R$ consists of a stationary, positive component, indicated by the red shaded area, and a fast, negative component with a decay time of 250 ± 10 ps, indicated by the blue shaded area. Spatial scans taken across the antenna at pump−probe delays of −20 ps (red dots) and 5 ps (black diamonds) are shown in Figure 1e. These scans, as well as the two-dimensional image of Figure 1c showing only the fast (blue) component, reveal that the fast pump−probe signal is only present at the position of the nanoantenna.

To further analyze the linear and nonlinear optical response of ITO without antennas, we performed spectrally resolved reflectivity and pump−probe experiments at a distance 5 μm away from the antenna structures. The inset of Figure 2a shows the experimental refectivity spectra of the low- (blue triangles) and high-conductivity (red dots) ITO layers. The reflectivity can be modeled using a simple Drude model description[28] including the

dx.doi.org/10.1021/nl200901w |*Nano Lett.* XXXX, XXX, 000–000

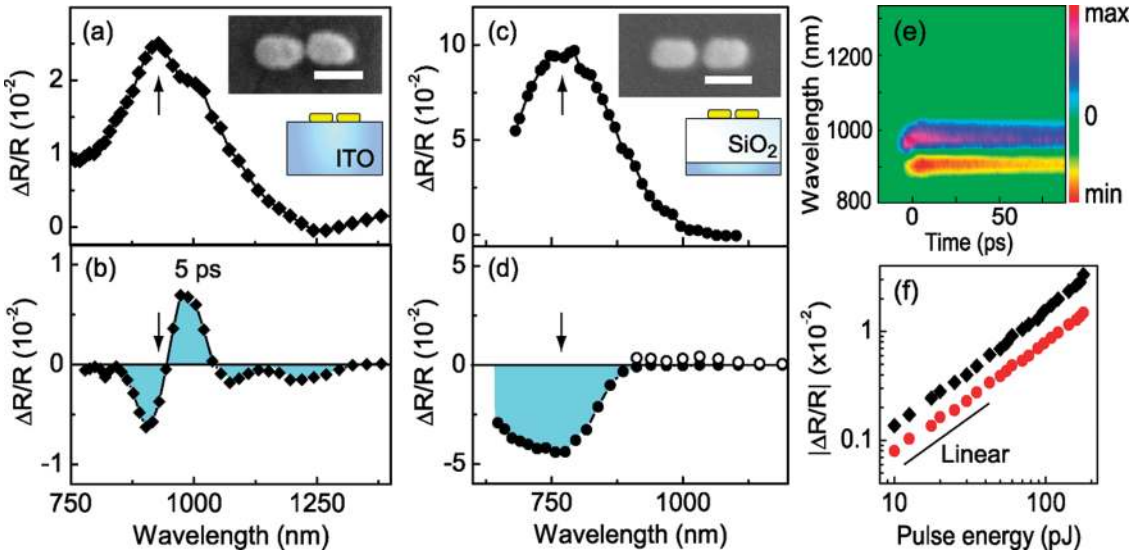

Figure 3. (a) Extinction spectrum and (b) Fast nonlinear response of nanoantenna with 20 nm gap embedded in high-conductivity ITO at 180 pJ. Vertical arrows indicate maximum of the antenna resonance. (c, d) Same for antenna with 30 nm gap on a SiO_2 spacer on low-conductivity ITO. The white dots indicate the positive amplitude of vibrational modes on the right-hand side of the antenna resonance. Insets (a, c) SEM images, scale bars 200 nm. (e) Time-resolved spectrum of nonlinear response for antenna a. (f) Dependence of the slow heat component (red circles) and the fast component (black diamonds) of $|\Delta R/R|$ on pump energy for antenna of (a), at 980 nm wavelength.

Table 1. Values for the Electron Density *N*, Pump-Induced Change of the Electron Density Δ*N*, and Calculated Value of the Nonlinear Coefficient n_2 at 1000 nm Wavelength for the Pure ITO Substrates as Well as for the Nanoantenna−ITO Hybrid of Figure 3a,b

	low-cond ITO	high-cond ITO	antenna−ITO hybrid
N (cm^{-3})	7.3×10^{20}	9.6×10^{20}	9.6×10^{20}
$-\Delta N$ (cm^{-3})	5.4×10^{16}	2.1×10^{18}	6.0×10^{19}
n_2 (cm^2/W)	4.0×10^{-14}	1.6×10^{-12}	5.9×10^{-11}

experimental dielectric response of ITO[29]

$$\tilde{\varepsilon}_{ITO}(\omega) = \tilde{\varepsilon}_{exp}(\omega) - \left(\frac{\omega_{pl}}{\omega}\right)^2 \frac{1}{1 + i(\omega\tau_D)^{-1}} \qquad (1)$$

where $\omega_{pl} = (Ne^2/\varepsilon_0 m^*)^{1/2}$ denotes the plasma frequency, with N the free electron density, $m^* = 0.4m_e$ the effective electron mass, and $\tau_D = 5 \times 10^{-15}$ s the Drude relaxation time of ITO.[25] Fits to the experimental data were obtained using a multilayer reflectivity model,[30] including the ITO film thickness, yielding electron densities of $9.6 \pm 0.1 \times 10^{20}$ cm^{-3} for the high-conductivity ITO and $7.3 \pm 0.1 \times 10^{20}$ cm^{-3} for the low-conductivity ITO sample (lines in inset Figure 2a).

The ITO reflectivity shows a transition from dielectric to metallic response, defined by the transition from positive to negative real part of ε. This behavior is also observed in the nonlinear reflectivity changes as shown in Figure 2a, representing the slow, stationary nonlinear component. The differential reflectivity $\Delta R/R$ can be calculated from the Drude model eq 1 through the shift of the plasmon resonance frequency $\Delta\omega_p = (\omega_p/2N)\Delta N$ for small changes in the carrier density ΔN. The general features of the experimental spectra for both ITO layers are reproduced well (lines in Figure 2a), apart from some discrepancy at longer wavelengths. The bipolar shape is attributed to the red shift of the bulk plasmon frequency, where the zero crossing in Figure 2a corresponds to the minimum in the Fresnel reflection at the air−ITO interface, given by $\tilde{\varepsilon}_{ITO} \simeq \varepsilon_{air}$. The fitted spectra show a decrease of the electron density ΔN of $(-2.1 \pm 0.1) \times 10^{18}$ cm^{-3} and $(-5.4 \pm 0.2) \times 10^{16}$ cm^{-3} for the high- and low-conductivity samples, respectively, at a pump energy of 180 pJ. Similar to the instantaneous Kerr effect,[31,32] the noninstantaneous free-carrier nonlinearity can be described by a nonlinear coefficient n_2 representing the ratio of the refractive index change to pump intensity. Table 1 shows resulting values of n_2 at a wavelength of 1000 nm. The value of n_2 for the low-conductivity ITO is of the same order as the Kerr-nonlinearity determined for ITO films with a similar electron density.[32] For the high-conductivity ITO, the free-carrier nonlinearity is significantly higher due to the strong dispersion of the free-carrier nonlinearity near the plasma frequency as observed in Figure 2a and the larger ΔN resulting from stronger pump absorption at 532 nm.

The spectrally resolved nonlinear response of the nanoantenna−ITO hybrid of Figure 1 is shown in Figure 2b, where we have plotted the $\Delta R/R$ amplitudes at delay times of −20 ps (red circles) and 5 ps (black diamonds). Clearly, the stationary component (red area) closely resembles the pure ITO response without the nanoantenna. We attribute this part to a background signal of ITO in the focal spot, which is unrelated to the nanoantenna. The fast component (blue areas) shows a bipolar shape centered at the antenna dipole resonance, shown in Figure 3a (vertical arrow). Given that the antenna covers a fraction of only several percent of the probe spot, the equal magnitude of the antenna and ITO signals shows that the antenna nonlinear response is an order of magnitude larger than that of the pure ITO, as will be quantified further below. A similar response was observed for antennas on an ITO substrate as for antennas which were fully covered with an ITO top layer. Also for the transverse polarization an antenna mode was found, which showed a similar nonlinear resonance shift as the longitudinal mode shown here.

dx.doi.org/10.1021/nl200901w |*Nano Lett.* XXXX, XXX, 000–000

In order to establish whether the pump−probe nonlinear response can be attributed to a gold, ITO, or hybrid antenna−ITO nonlinearity, we performed additional experiments using antennas which were separated from the ITO by a 100 nm SiO_2 spacer layer. In Figure 3b,d we compare the fast (i.e., background subtracted) response of two nanoantennas grown on high-conductivity ITO and on SiO_2. Corresponding optical extinction spectra are shown in panels a and c of Figure 3, for polarizations parallel to the antenna axis. We find that antennas on ITO generally have a smaller cross section compared to antennas on SiO_2, which is attributed to the different substrate permittivities in the spectral region of interest. Panels b and d of Figure 3 show a very different behavior for the nonlinear reflectivity of the two antennas. For the antenna on SiO_2, a predominantly negative $\Delta R/R$ is found, which is consistent with bleaching of the surface plasmon resonance by nonequilibrium heating of conduction electrons in the gold.[33−35] The open circles in Figure 3d indicate slightly positive values which are caused by acoustic oscillations, as will be discussed further below. A complete time- and wavelength-dependent picture of the nonlinear modulation for the antenna−ITO hybrid is shown in Figure 3e. The dependence of the pump−probe reflectivity on the pump energy per pulse is shown in Figure 3f. Both the stationary (red dots) and the fast (black diamonds) components show a linear dependence on pump power, which is expected for a third-order nonlinearity where the refractive index change is proportional to the pump intensity times the nonlinear coefficient n_2.

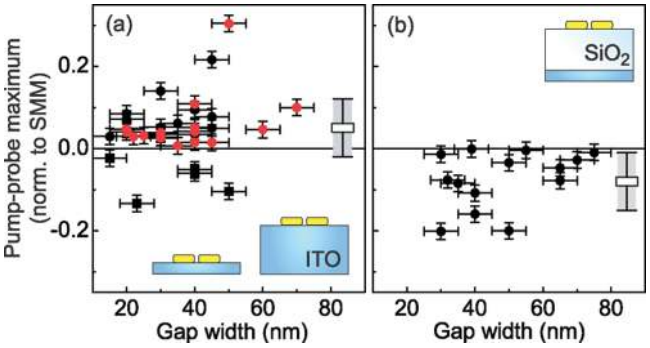

Figure 4. Statistics of the maximum pump probe effect normalized by the spectral maximum for (a) high-conductivity (black circles) and low-conductivity ITO (red circles) as well as for (b) a SiO_2 spacer between the antenna and low-conductivity ITO. ITO layers are blue; SiO_2 layers are white. The pumping energy is 80 pJ for all measurements. Gray shaded bars denote statistical averages and standard deviations for all antennas.

A full statistical analysis of the behavior of a number of antennas on the different samples is shown in Figure 4, where we have plotted the maximum value of the nonlinear $\Delta R/R$ signal at a pump energy of 80 pJ. Here the nonlinear signals were normalized to the maximum of the spatial modulation signal in order to normalize variations in antenna polarizability. A positive value is reported for antennas showing a bipolar response, while a negative value represents a unipolar bleaching signal. The statistical analysis confirms the observation of Figure 3 that a qualitatively different response is found for the antenna−ITO hybrids as for the antennas on SiO_2. Four antennas on high-conductivity ITO did not show the reported resonance shift but rather showed a transient bleaching response. Although a detailed understanding of the variations observed in Figure 4 is lacking, we expect these may be related to local variations of the samples, including nanoantenna−substrate attachment, roughness, and polycrystallinity of the ITO. The measurements do not show a dependence on antenna gap size, indicating that the effects are not critically dependent on antenna gap filling.[17] This is consistent with the limited effect of full ITO coverage on the nonlinear response. The gray shaded bars denote statistical averages and standard deviations for all antennas, yielding values of 0.05 ± 0.06 and -0.1 ± 0.08 for the antennas on ITO and on SiO_2, respectively. As we used relatively moderate pump powers to obtain the statistics of Figure 4, the modulation depths will be 2.5 times larger for the highest pump powers used in Figure 3.

The above experimental results indicate that the fast modulation of nanoantennas on ITO is directly related to nonlinear refractive index changes in the ITO substrate. As a starting point in our analysis of the ITO−antenna interaction, we calculate the response of a plasmonic nanoantenna to a modification of the ITO free-carrier density using FDTD simulations. We consider a rectangular dimer nanoantenna with dimensions of $200 \times 120 \times 25$ nm^3

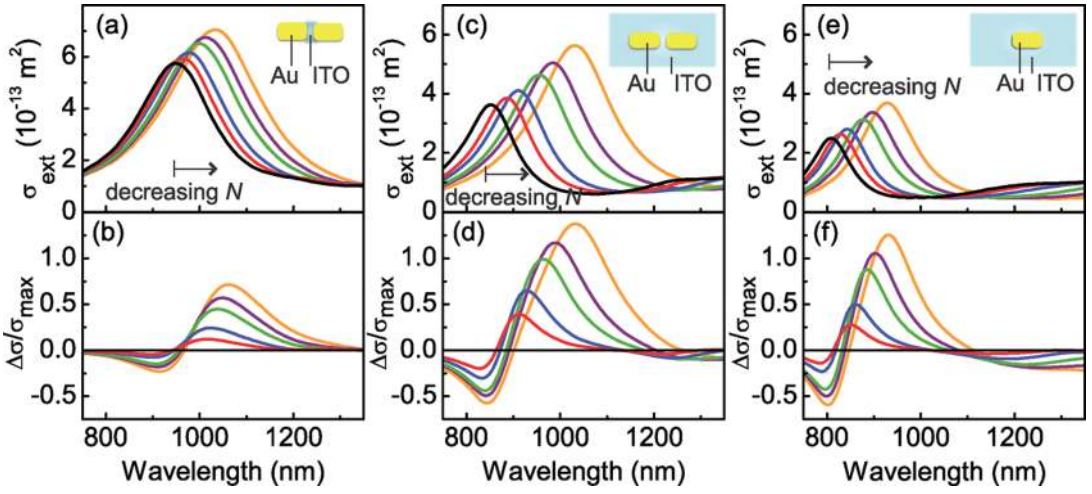

Figure 5. (a) Simulated extinction spectra for an antenna with ITO only in the gap with the same dimensions as the antenna in Figure 2 with arm length 200 nm, arm width 120 nm, height 25 nm, and gap size 20 nm with FDTD simulations at different carrier concentrations: 9.6 (black), 9.0 (red), 8.0 (blue), 7.0 (green), 6.0 (magenta), and 5.0 (orange) $\times 10^{20}$ cm^{-3}. (b) Corresponding differential signal. (c, d) Same as (a, b), but for an antenna completely embedded in ITO, comparable to the antenna in Figure 2. (e, f) Same but for a single nanorod embedded in ITO.

dx.doi.org/10.1021/nl200901w |Nano Lett. XXXX, XXX, 000–000

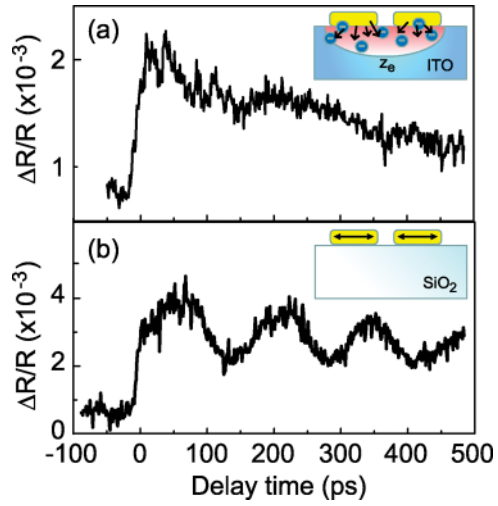

Figure 6. Experimental time-resolved reflectivity, at 1050 nm wavelength, of single nanoantennas on high-conductivity ITO (a) and on SiO_2. (b) Inset: mechanisms showing fast electron injection from the gold into the depleted ITO (a) and energy relaxation in the isolated gold antenna on SiO_2 (b), exciting the coherent vibrational modes of the nanoparticle.

for the individual arms and a gap width of 20 nm. The effect of the ITO distribution is assessed by comparing a geometry in which ITO is present only in the antenna gap with one where the antenna is fully embedded in ITO (see insets of Figure 5a,c). Single-antenna extinction cross sections are shown in panels a and c of Figure 5 for various ITO free-carrier densities between (5.0 and 9.6) $\times$ 10^{20} cm^{-3}. A decrease of the free-carrier density N is associated with a red shift of the antenna dipole resonance. Notice that this happens in the regime in which the ITO is dielectric, where an increase in the free-carrier density results in an decrease of the refractive index and in addition a screening of the capacitive antenna interaction.[17]

Starting from the experimentally determined carrier density of 9.6 $\times$ 10^{20} cm^{-3}, differential pump–probe spectra are obtained as shown in Figure 5b,d for pump-induced changes of the carrier density. The magnitude and spectral shape of the theoretical curves matches well our experimental data for a change in carrier density of $\Delta N = -6 \times 10^{19}$ cm^{-3}. This carrier reduction is one and two orders of magnitude larger than the stationary variations measured for the high- and low-conductivity ITO substrates in absence of antennas, respectively (see Table 1). The nonlinear coefficient n_2 for the antenna–ITO hybrid is found to be 5.9 $\times$ 10^{-11} cm^2/W, or 1.4 $\times$ 10^{-8} esu, which is 36 times larger than that for ITO without nanoantennas. Thus, the nanoantenna is shown to act as a sensitizer for the ITO free-carrier nonlinearity. We note that the free-carrier nonlinearity of isolated gold nanoparticles can reach as high as 10^{-7} esu,[36,37] which is however governed by its imaginary part resulting in plasmon bleaching as observed in Figure 3d.

While the antenna resonance clearly is sensitive to dielectric gap loading,[14] no qualitative difference is observed with the fully embedded antenna, which shows the largest resonance shift. We also performed calculations for antennas on an ITO substrate, giving qualitatively similar results as for the two cases presented here. The effect of capacitive arm coupling is assessed by comparing also the response of an individual gold nanorod of the same length as the antenna arm. Panels e and f of Figure 5 show that the shift of the resonance for a single rod is smaller than that for the coupled antenna arms; however, the effect of shifting with free carrier concentration can be also observed clearly in this single-antenna case. This confirms the nature of the shift as due to the antenna–ITO hybrid response. We note that the increase of the extinction toward long wavelengths can be attributed to absorption in the ITO substrate, which scales proportional to the amount of ITO material present in the model. The oscillations in the pump–probe signal observed in this region in Figure 5d, which are also found in our experimental data of Figure 3b, result from the changes in the ITO free-carrier density directly surrounding the antenna.

The order-of-magnitude difference in free-carrier modulation obtained for the antenna–ITO hybrid as compared to pure ITO suggests an effect of the nanoantenna on the local carrier density. Furthermore, the pronounced difference in the $\Delta R/R$ pump–probe response for the antennas on ITO and SiO_2 in Figure 3 indicates a difference in mechanism underlying the antenna nonlinear response. This interpretation is supported by further evidence gained from the presence of vibrational modes, as shown in Figure 6. It is well-known that for colloidal gold nanoparticles, rapid energy relaxation of photoexcited electrons to the lattice results in a coherent mechanical oscillation of the nanoparticle. We observed these vibrational modes (Figure 6b) for a large number of antennas on SiO_2, as well as on low-conductivity ITO, but not for antennas on high-conductivity ITO (Figure 6a). Of 17 antennas on low-conductivity ITO, we found vibrational modes on 11 (64.7%), while 15 out of 24 antennas (62.5%) on SiO_2 showed acoustic vibrations. For antennas on high-conductivity ITO, on the other hand, we found no vibrations for all 19 antennas under study. A faster damping of the vibrational modes of the gold antenna on ITO than on SiO_2 would be expected given the acoustic impedances (Z_{Au} = 6.2 $\times$ 10^7, Z_{ITO} = 5.6 $\times$ 10^7, Z_{SiO_2} = 3.5 $\times$ 10^7 kg m^{-2} s^{-1}). However, the acoustic impedance cannot explain the incongruity between low- and high-conductivity ITO.

The absence of vibrational modes supports our interpretation that there must be a fundamental difference in the energy transfer mechanism for the two substrates. To explain all the above observations, we propose a mechanism based on fast injection of hot electrons from the photoexcited gold into the ITO substrate, followed by thermalization and a local depletion of the ITO. This process is facilitated by the high dc conductance of ITO combined with a good electrical contact between the antenna and substrate. The hot-electron diffusion length z_e for a gold film can be calculated as $z_e = (\kappa_e/g)^{1/2} \simeq 126$ nm. Here we used the electronic thermal conductivity $\kappa_e \simeq 317$ W m^{-1} K^{-1} and the electron–phonon coupling constant $g = 2.0 \times 10^{16}$ W m^{-3} K^{-1} of gold.[38] Assuming a good Ohmic conductance of the antenna–ITO interface, hot-electron injection within the electron–phonon relaxation time thus results in a rapid heating of the ITO substrate directly surrounding the antenna. We calculate the instantaneous temperature rise in a cube of ITO of 200 $\times$ 100 $\times$ 100 nm^3 dimensions. The instantaneous temperature rise follows as $\Delta T = \sigma_a F/c_V V \simeq 270$ °C. Here we used the calculated antenna absorption cross section at 532 nm, σ_a = 2.4 $\times$ 10^{-14} m^2, the pump fluence F = 57 J m^{-2}, and the heat capacity of ITO c_V = 2.58 $\times$ 10^6 J m^{-3} K^{-1}.[42] These values for F and σ_a correspond to a switching energy of 1.4 pJ.

Fast local heating of the ITO surrounding the nanoantenna, following hot-electron injection, results in a net migration of free-carriers due to thermal diffusion and a space charge formation

dx.doi.org/10.1021/nl200901w |Nano Lett. XXXX, XXX, 000–000

analogous to the photo-Dember effect.[39] The decay of the pump–probe antenna modulation is governed by cooling of the heated area on a time scale of ~250 ps.[40] The high repetition frequency of our setup results in a stationary background temperature over a larger, micrometer-sized area,[41] which provides the pure ITO signal in Figures 1 and 2. This background temperature is found to be $\Delta T_0 = 2\sigma_a I/4\pi\kappa r = 10$ °C at a distance $r \sim 0.2$ μm, where we used the average laser intensity $I = 3 \times 10^9$ W m^{-2} and the thermal conductivity of ITO $\kappa = 5.9$ W m^{-1} K^{-1}.[42]

In conclusion, we have demonstrated all-optical control of nanoantennas on ITO. We identify a hybrid picosecond nonlinear response involving fast hot-electron injection from the gold antenna, followed by thermalization and a local reduction of the ITO free-carrier density. Our work shows that plasmon-mediated hot-electron injection provides new functionality in controlling the optical properties of materials at the nanoscale, which is of fundamental importance as it opens a path for new ultrafast devices and for exploring combinations of new materials to produce all-optical switching. By exploiting the large free-carrier nonlinearity of ITO around the bulk plasmon frequency, hot-electron injection provides a large modulation of the antenna dipole resonance wavelength. The transparent conductive oxide ITO is shown to be a promising nonlinear material for nanophotonic switches, supporting earlier work on electro-optical modulation.[22] Future investigations will have to address the origins of the large differences between individual antennas, which may be related to structural variations in the ITO on the nanoscale and to variations in nanofabrication, especially the gold–ITO contact. Currently the applied laser intensities in our studies are limited by thermal instability and laser-induced damage; however calculations predict that further improvement of the carrier depletion by 1 order will provide even larger modulation of the plasmon modes. Future research may explore combinations of optical and electrical[22] control of antenna–ITO hybrids to achieve this goal. Ultimately, order-unity modulation of the plasmonic antenna modes in an all-solid-state configuration will enable important new applications in switching of information channels,[4] control of nonlinear optical processes,[43] and radiative decay engineering.[44]

AUTHOR INFORMATION

Corresponding Author

*E-mail: O.Muskens@soton.ac.uk.

ACKNOWLEDGMENT

The authors acknowledge Z. Webber and M. A. Bampton for their technical support. O.L.M. acknowledges support from EPSRC through Grant EP/H019669/1. P.A. and J.A. acknowledge funding from the ETORTEK project inanoGUNE from the Basque Government and project FIS2007-66711-C01-01 of the Spanish Ministry of Innovation and Science.

REFERENCES

(1) Mühlschlegel, P.; Eisler, H.-J.; Martin, O. J. F.; Hecht, B.; Pohl, D. W. *Science* **2005**, *308*, 1607–1609.
(2) Bharadwaj, P.; Deutsch, B.; Novotny, L. *Adv. Opt. Photonics* **2009**, *1*, 438–483.
(3) Brongersma, M. L.; Shalaev, V. M. *Science* **2010**, *328*, 440–441.
(4) Miller, D. A. B. *Nat. Photonics* **2010**, *4*, 3–5.
(5) Lei, D. Y.; Appavoo, K.; Sonnefraud, Y.; Haglund, R. F.; Maier, S. A. *Opt. Lett.* **2010**, *35*, 3988–3990.
(6) Wurtz, G. A.; Pollard, R.; Zayats, A. V. *Phys. Rev. Lett.* **2006**, *97*, 057402.
(7) Huang, F.; Baumberg, J. J. *Nano Lett.* **2010**, *10*, 1787–1792.
(8) López, R.; Feldman, L. C.; Haglund, R. F. *Phys. Rev. Lett.* **2004**, *93* (177403), 1–4.
(9) MacDonald, K. F.; Zheludev, N. I. *Laser Photonics Rev.* **2010**, *4*, 562–567.
(10) Pacifici, D.; Lezec, H. J.; Atwater, H. A. *Nat. Photonics* **2007**, *1*, 402–406.
(11) Dionne, J. A.; Diest, K.; Sweatlock, L. A.; Atwater, H. A. *Nano Lett.* **2009**, *9*, 897–902.
(12) Wiederrecht, G. P.; Hall, J. E.; Bouhelier, A. *Phys. Rev. Lett.* **2007**, *98*, 083001.
(13) MacDonald, K. F.; Sámson, Z. L.; Stockman, M. I.; Zheludev, N. I. *Nat. Photonics* **2008**, *3*, 55–58.
(14) Alù, A.; Engheta, N. *Nat. Photonics* **2008**, *2*, 307–310.
(15) Wurtz, G. A.; Pollard, R.; Hendren, W.; Wiederrecht, G. P.; Gosztola, D. J.; Podolskiy, V. A.; Zayats, A. V. *Nat. Nanotechnol.* **2011**, *6*, 107–111.
(16) Nikolaenko, A. E.; De Angelis, F.; Boden, S. A.; Papasimakis, N.; Ashburn, P.; Di Fabrizio, E.; Zheludev, N. I. *Phys. Rev. Lett.* **2010**, *104*, 153902.
(17) Large, N.; Abb, M.; Aizpurua, J.; Muskens, O. L. *Nano Lett.* **2010**, *10*, 1741–1746.
(18) Kossyrev, P. A.; Yin, A.; Cloutier, S. G.; Cardimona, D. A.; Huang, D.; Alsing, P. M.; Xu, J *Nano Lett.* **2005**, *5*, 1978–1981.
(19) Bertholot, J.; Bouhelier, A.; Huang, C.; Margueritat, J.; Colas-des-Francs, G.; Finot, E.; Weeber, J.-C.; Dereux, A.; Kostcheev, S.; Ibn El Ahrach, H.; Baudrion, A.-L.; Plain, J.; Bachelot, R.; Royer, P.; Wiederrecht, G. P. *Nano Lett.* **2009**, *9*, 3914–3919.
(20) Fan, J. A.; Wu, C.; Bao, K.; Bao, J.; Bardhan, R.; Halas, N. J.; Manoharan, V. N.; Nordlander, P.; Shvets, G.; Capasso, F. *Science* **2010**, *328*, 1135–1138.
(21) West, P.; Ishii, S.; Naik, G.; Emani, N.; Shalaev, V. M.; Boltasseva, A. *Laser Photonics Rev.* **2010**, *4*, 795–808.
(22) Feigenbaum, E.; Diest, K.; Atwater, H. A. *Nano Lett.* **2010**, *10*, 2111–2116.
(23) Granqvist, C. G.; Hultaker, A. *Thin Solid Films* **2002**, *411*, 1–5.
(24) Ray, S.; Banerjee, R.; Basu, N.; Batabyal, A. K.; Barua, A. K. *J. Appl. Phys.* **1983**, *54*, 3497–3501.
(25) Losego, M. D.; Efremenko, A. Y.; Rhodes, C. L.; Cerruti, M. G.; Franzen, S.; Maria, J.-P. *J. Appl. Phys.* **2009**, *106*, 024903.
(26) Arbouet, A.; Christofilos, D.; Del Fatti, N.; Vallé, F.; Huntzinger, J. R.; Arnaud, L.; Billaud, P.; Broyer, M. *Phys. Rev. Lett.* **2004**, *93*, 127401.
(27) Muskens, O. L.; Del Fatti, N.; Vallé, F.; Huntzinger, J. R.; Broyer, M. *Appl. Phys. Lett.* **2006**, *88*, 063109.
(28) Zhang, J.; Atay, T.; Nurmikko, A. V. *Nano Lett.* **2009**, *9*, 519–524.
(29) Palik, E. D. *Handbook of Optical Constants of Solids*; Academic Press: Boston, 1991.
(30) Brewer, S. H.; Franzen, S. *J. Phys. Chem. B* **2002**, *106*, 12986–12992.
(31) Lenz, G.; Zimmermann, J.; Katsufuji, T.; Lines, M. E.; Hwang, H. Y.; Spalter, S.; Slusher, R. E.; Cheong, S. -W.; Sanghera, J. S.; Aggarwal, I. D. *Opt. Lett.* **2000**, *25*, 254–256.
(32) Elim, H. I.; Ji, W; Zhu, F *Appl. Phys. B: Laser Opt.* **2006**, *82*, 439–442.
(33) Link, S.; El-Sayed, M. A. *J. Phys. Chem. B* **1999**, *103*, 8410–8426.
(34) Voisin, C.; Christofilos, D.; Loukakos, P. A.; Del Fatti, N.; Vallée, F.; Lermé, J.; Gaudry, M.; Cottancin, E.; Pellarin, M.; Broyer, M. *Phys. Rev. B* **2004**, *69*, 195416.
(35) Hartland, G. V. *Chemical Science* **2010**, *1*, 303–309.
(36) Hache, F.; Ricard, D.; Flytzanis, C.; Kreibig, U. *Appl. Phys. A: Solids Surf.* **1988**, *47*, 347–357.
(37) Inouye, H.; Tanaka, K.; Tanahashi, I.; Hirao, K *Phys. Rev. B* **1998**, *57*, 11334–11340.
(38) Gusev, V. E.; Wright, O. B. *Phys. Rev. B* **1998**, *57*, 2878–2888.
(39) Schroeder, W. A.; Stark, T. S.; Smirl, A. L. *Opt. Lett.* **1991**, *16*, 989–991.

(40) Juvé, V.; Scardamaglia, M.; Maioli, P.; Crut, A.; Merabia, S.; Joly, L.; Del Fatti, N.; Vallée, F. *Phys. Rev. B* **2009**, *80*, 195406.
(41) Hurley, D. H.; Wright, O. B.; Matsuda, O.; Shinde, S. L. *J. Appl. Phys.* **2010**, *107*, 023521.
(42) Ashida, T; Miyamura, A; Oka, N; Sato, Y.; Yagi, T.; Taketoshi, N.; Baba, T; Shigesato, Y. *J. Appl. Phys.* **2009**, *105*, 073709.
(43) Utikal, T; Stockman, M. I.; Heberle, A. P.; Lippitz, M.; Giessen, H. *Phys. Rev. Lett.* **2010**, *104*, 113903.
(44) Chen, Y.; Lodahl, P.; Koenderink, A. F. *Phys. Rev. B* **2010**, *82*, 081402(R).